Insights into transducer-plane streaming patterns in thin-layered acoustofluidic devices

Junjun Lei,* Martyn Hill† and Peter Glynne-Jones‡
Faculty of Engineering and the Environment, University of Southampton, Southampton, SO17 1BJ, UK
(Received xxxx)

While classical Rayleigh streaming, whose circulations are perpendicular to the transducer radiating surfaces, is well-known, transducer-plane streaming patterns, in which vortices circulate parallel to the surface driving the streaming, have been less widely discussed. Previously, a four-quadrant transducer-plane streaming pattern has been seen experimentally and subsequently investigated through numerical modelling. In this paper, we show that by considering higher order three-dimensional cavity modes of rectangular channels in thin-layered acoustofluidic manipulation devices, a wider family of transducer-plane streaming patterns are found. As an example, we present a transducer-plane streaming pattern, which consists of eight streaming vortices with each occupying one octant of the plane parallel to the transducer radiating surfaces, which we call here *eight-octant transducer-plane streaming*. An idealised modal model is also presented to highlight and explore the conditions required to produce rotational patterns. It is found that both standing and travelling wave components are typically necessary for the formation of transducer-plane streaming patterns. In addition, other streaming patterns related to acoustic vortices and systems in which travelling waves dominate are explored with implications for potential applications.

DOI:

I. INTRODUCTION

Acoustic streaming is steady fluid motion driven by the absorption of acoustic energy due to the interaction of acoustic waves with the fluid medium or its solid boundaries. Understanding the driving mechanisms of acoustic streaming patterns within acoustofluidic devices is important in order to precisely control it for the enhancement or suppression of acoustic streaming for applications such as particle/cell manipulation [1-8], heat transfer enhancement [9-12], non-contact surface cleaning [13-17], microfluidic mixing [18-27], and transport enhancement [28-35].

In most bulk micro-acoustofluidic particle and cell manipulation systems of interest, the acoustic streaming fields are dominated by boundary-driven streaming [36], which is associated with acoustic dissipation in the viscous boundary layer [37]. Theoretical work on boundary-driven streaming was initiated by Rayleigh [38], and developed by a series of modifications for particular cases [39-44], which have paved the fundamental understanding of acoustic streaming flows.

While Rayleigh streaming patterns (which have streaming vortices with components perpendicular to the driving boundaries) have been extensively studied [45-48], we have recently explored the mechanisms behind four-quadrant transducer-plane streaming [49] which generates streaming vortices in planes parallel to the driving boundary, and modal Rayleigh-like streaming [50] in which vortices have a roll size greater than the quarter wavelength of the main acoustic resonance and are driven by *limiting velocities* (the value of the streaming velocity just outside the boundary layer [41,49], on the boundaries perpendicular to the axis of the main acoustic resonance). The expressions for the limiting velocities have terms corresponding to acoustic velocity gradients along each coordinate axis. Depending on which of these is dominant, different acoustic streaming patterns arise in thin-layered acoustofluidic devices [50], corresponding to the rotational and irrotational features of, respectively, the active and reactive intensity patterns in acoustic fields [51]. The defining feature of transducer-plane streaming is that its vorticity is driven by vorticity in the limiting velocity patterns themselves.

In this paper, we first investigate higher order transducer-plane streaming patterns in thin-layered acoustofluidic manipulation devices. "Thin-layered" devices are defined here as resonators in which the thickness of the fluid layer (in the direction of the acoustic axis) is less that $1/20^{th}$ of its lateral dimensions [50] and of the order of half an acoustic wavelength. We introduce a new boundary-driven streaming pattern observed in a thin-layered glass capillary device and then investigate the underlying physics of transducer-plane streaming with an analytical model in order to gain insights into the contributions of standing and travelling wave components, respectively.

II. *EIGHT-OCTANT TRANSDUCER-PLANE STREAMING*

The experiments were performed in a transducer-capillary device using micro particle image velocimetery (μpiv) system as shown in FIG. 1(a), similar to those we used previously [49,50] (see [52] and details in the supplemental material [53]). This acoustofluidic system is of interest as it is used elsewhere in a blood and bacterial capture device [1,2]. The measurements were performed within xy horizontal planes (see FIG. 1(a)). The investigation area was above the transducer radiating surface. FIG. 1(c) shows the streaming pattern observed (at a frequency of 2.498 MHz), where an *eight-octant*, steady acoustic streaming pattern in which each vortex occupies approximately one octant of the viewed xy horizontal plane. The plane of these vortices is parallel to the transducer radiating surface (i.e., perpendicular to the axis of the main standing wave in the z direction), as is the case for the four-quadrant transducer-plane streaming we have presented previously [49], but in a different plane to the vortices observed in Rayleigh streaming [38]. Detailed fluid motion can be seen from in FIG. 1(d), where μpiv results of the streaming field in the third quadrant are presented. It can be seen that vortices are generated each of which occupies one octant.

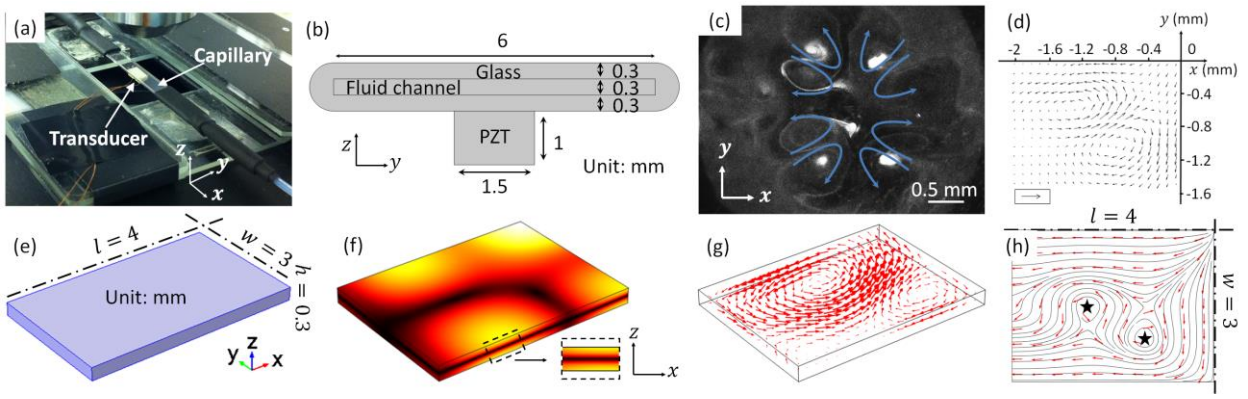

FIG. 1. (a) The experimental acoustofluidic particle manipulation device, where, to connect the capillary to plastic tubing, heat shrinkable tubing (black) were used at the two ends of the capillary; (b) cross section of the device; (c) a photographic image of the distribution of beads (radius of 1 μm) in the fluid after some minutes of streaming, where a main *eight-octant transducer-plane streaming* pattern can be seen in which beads have agglomerated near the center of the streaming vortices and at the center of the device; (d) μpiv measurements of the eight-octant transducer-plane streaming field in the third quadrant shown in (c) at a voltage of 30 Vp-p, where the arrow in the box shows a reference velocity of 20 μm/s; (e) the considered 3D model ($4 \times 3 \times 0.3$ mm^3), where the dash-dot lines show the symmetry planes; (f) the first-order acoustic pressure field on all surfaces; (g) the 3D acoustic streaming velocity field, where velocity vectors are shown at two heights within the chamber (z positions of one third and two thirds of the chamber height); and (h) the active intensity (i.e., the limiting velocity field) on the driving boundaries ($z = \pm h/2$), where the five-pointed stars show the points of minimum pressure amplitude and normalized arrows are used to show the flow directions.

To understand the driving mechanism of this *eight-octant transducer-plane streaming* pattern, the finite element package COMSOL [54] was used to model the acoustic and streaming fields in the experimental device. In this work, we have applied the limiting velocity method [41] based on the perturbation method [44] to model the 3D outer streaming fields in the capillary device. We have previously established the viability of this method for solving 3D boundary-driven streaming fields in thin-layered acoustofluidic manipulation devices [48-50] and in vibrating plate systems [55].

III. Numerical model

The full numerical procedure can be split into three steps. Firstly, the first-order acoustic fields within the devices were modelled using the COMSOL '*Pressure Acoustics, Frequency Domain*' interface, which solves the harmonic, linearized acoustic problems, taking the form:

$$\nabla^2 p_1 = -\frac{\omega^2}{c^2} p_1, \tag{1}$$

where p_1 is the complex acoustic pressure, ω is the angular frequency and c is the sound speed in the fluid. As the device is symmetric to the centre, only a quarter of the fluid channel was modelled here for numerical efficiency and the model is located within coordinates: $-l \le x \le 0, -w \le y \le 0, -h/2 \le z \le h/2$ (see FIG. 1(e)). Edges $x = 0$ and $y = 0$ were set as symmetric boundary conditions. We excited the standing wave field through a '*normal acceleration*' boundary condition on the bottom surface as published previously [49,50]. Surface $x = -l$ was set as a plane wave radiation condition in order to simulate the loss of acoustic energy at the two ends of the fluid channel. The remaining walls were modelled using sound reflecting boundary conditions as these are water-glass interfaces and we are working at frequencies away from resonances of these walls.

Secondly, the limiting velocities at all boundaries were calculated as a function of the first-order acoustic velocity fields. On planar surfaces normal to z, the limiting velocity equations on the driving boundaries ($z = \pm h/2$) take the form [49]:

$$u_L = \frac{-1}{4\omega}\mathrm{Re}\left\{q_x + u_1^*\left[(2+i)\nabla\cdot\boldsymbol{u_1} - (2+3i)\frac{dw_1}{dz}\right]\right\}, \tag{2a}$$

$$v_L = \frac{-1}{4\omega}\mathrm{Re}\left\{q_y + v_1^*\left[(2+i)\nabla\cdot\boldsymbol{u_1} - (2+3i)\frac{dw_1}{dz}\right]\right\}, \tag{2b}$$

$$q_x = u_1\frac{du_1^*}{dx} + v_1\frac{du_1^*}{dy}, \tag{2c}$$

$$q_y = u_1\frac{dv_1^*}{dx} + v_1\frac{dv_1^*}{dy}, \tag{2d}$$

where u_L and v_L are the two components of limiting velocities along coordinates x and y, Re represents the real part of a complex value, and u_1, v_1 and w_1 are components of the complex first-order acoustic velocity vector, $\boldsymbol{u_1}$, along the coordinates x, y and z, respectively. The superscript, $*$, represents the complex conjugate.

Finally, this limiting velocity method was used to model the acoustic streaming fields in this thin-layered acoustofluidic device using the COMSOL '*Creeping Flow*' interface. Outside of the acoustic boundary layer, the governing equations for the second-order streaming velocities, $\boldsymbol{u_2}$, and the associated pressure fields, p_2, are

$$\nabla p_2 = \mu\nabla^2\boldsymbol{u_2}, \tag{3a}$$

$$\nabla\cdot\boldsymbol{u_2} = 0, \tag{3b}$$

where μ is the dynamic viscosity of the fluid. Here, the bottom and top surfaces ($z = \pm h/2$) were considered as limiting velocity boundary conditions, surfaces $x = 0$ and $y = 0$ were symmetric conditions and the remaining surfaces were no-slip boundary conditions.

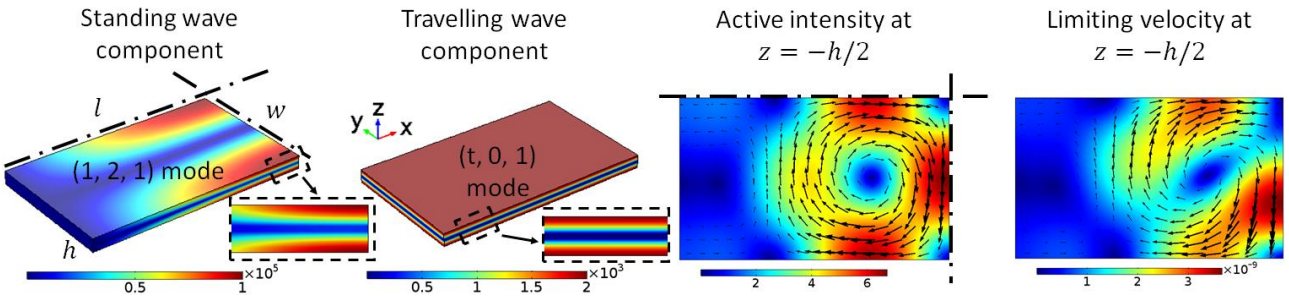

FIG. 2. The active intensity (W/m^2) and limiting velocity (m/s) fields at the driving boundaries for a combination of standing and travelling wave components (Pa). The phase difference between the standing and travelling wave components, $\varphi = -\pi/2$. The relationships between the four-quadrant transducer-plane streaming magnitudes, $|\boldsymbol{u_2}|$, the active intensity magnitudes $|\boldsymbol{I}|$, and the acoustic pressure amplitudes are shown in equation 5. Arrows in (c) and (d) show the corresponding vector fields.

The modeled acoustic pressure and acoustic streaming fields at the resonant frequency $f_r = 2.4973$ MHz (obtained from a frequency sweep to find the frequency which gives the maximum energy density in the cavity) in the 3D fluid volumes are shown in FIG. 1(f-g). It can be seen from FIG. 1(g) that this quadrant model contained two dominant streaming vortices with circulations parallel to the bottom surface (i.e., the transducer radiating surface), which compares well with the measured acoustic streaming vortices, shown in FIG. 1(d).

The acoustic pressure field is shown in FIG. 1(f), a mode with a half-wavelength in the z-direction of the model. The fields along the x and y axes have approximately one and a half- and one-wavelength variations respectively. The rotational components of transducer-plane streaming are closely linked to the active intensity field [49], which tends to circulate about pressure nodal points [51,56]. The modeled active intensity field in this case is shown in FIG. 1(h) and is consistent with this, showing rotation at the boundary about the two regions of minimum pressure amplitude on the surface. These vortices thus drive the eight-octant transducer-plane streaming patterns in the xy horizontal planes of the 3D fluid channels, with this higher order resonance producing a higher order eight-octant vortex pattern in the active sound intensity field in comparison with four-quadrant streaming.

IV. ANALYTICAL MODEL

We have previously presented results for transducer-plane streaming in acoustofluidic devices [50], showing that rotation in the active intensity is closely linked to the rotational patterns seen in experiments. What was not made clear previously was that a single standing wave mode does not exhibit this rotation of active intensity. To achieve rotational active intensity in a two-dimensional sound field it is typically necessary to have a line or point pressure minimum [56-58] This can result from the superposition of a travelling and standing wave (see below) or of two standing waves. This is supported with reference to our previous models [48-50], where we find that if the radiation boundary conditions (which allowed for the passage of energy across them, but still reflected a proportion of that energy to create combinations of standing and travelling waves), are replaced with rigid or free boundary conditions, the rotational patterns vanish. Hence in this section we create an analytical model to study the streaming patterns resulting from simple combinations of cavity modes and travelling modes for a case that generates the four-quadrant transducer-plane streaming patterns in order to obtain more insight into the relative significance of the travelling and standing wave components, and the effects of different modes and phase relationships.

In our model, the first-order acoustic pressure field, p_1, established in the fluid channel is decomposed into two components, a standing wave component, p_{1s}, and a travelling wave component (in the x-direction), p_{1t},

$$p_1 = p_{1s} + p_{1t}, \tag{4a}$$

$$p_{1s} = p_{0s}\cos(k_{xs}x)\cos(k_{ys}y)\sin(k_{zs}z)\,e^{i\omega t}, \tag{4b}$$

$$p_{1t} = p_{0t}e^{ik_{xt}x}\cos(k_{yt}y)\sin(k_{zt}z)\,e^{i(\omega t+\varphi)}, \tag{4c}$$

where subscripts s and t indicate the standing and travelling wave components respectively, p_0 is the acoustic pressure amplitude, ω is the angular frequency and φ indicates the phase difference between the standing and travelling wave components. The wave numbers in the x, y and z directions are k_x, k_y and k_z. Each wave number has both a standing and travelling wave component as indicated by the second s or t subscripts.

As discussed above the standing (cavity) mode components of equations 4 alone produce irrotational limiting velocity fields but the combination of travelling and standing wave components is the probable cause of the patterns seen, as borne out by the correspondence between modeled and experimental results. An example of the streaming field created by an acoustic vortex formed from the superposition of two standing wave modes is shown in FIG. S2 in the supplemental material [52]. It is interesting to note the applicability of the limiting velocity method in this case. Here we take the four-quadrant streaming pattern as an example (perhaps the simplest) to illustrate the roles of respectively the standing and travelling wave components [50]. The limiting velocity fields at the driving boundaries for various combinations of standing and travelling wave components were examined. It was found that the regular four-quadrant vortex pattern is obtained for a combination of the (1, 2, 1) standing wave mode and (t, 0, 1) travelling wave mode, shown in FIG. 2.

The corresponding patterns with other travelling wave components can be found in the supplemental material [52]. In a real device, combinations of these modes might be

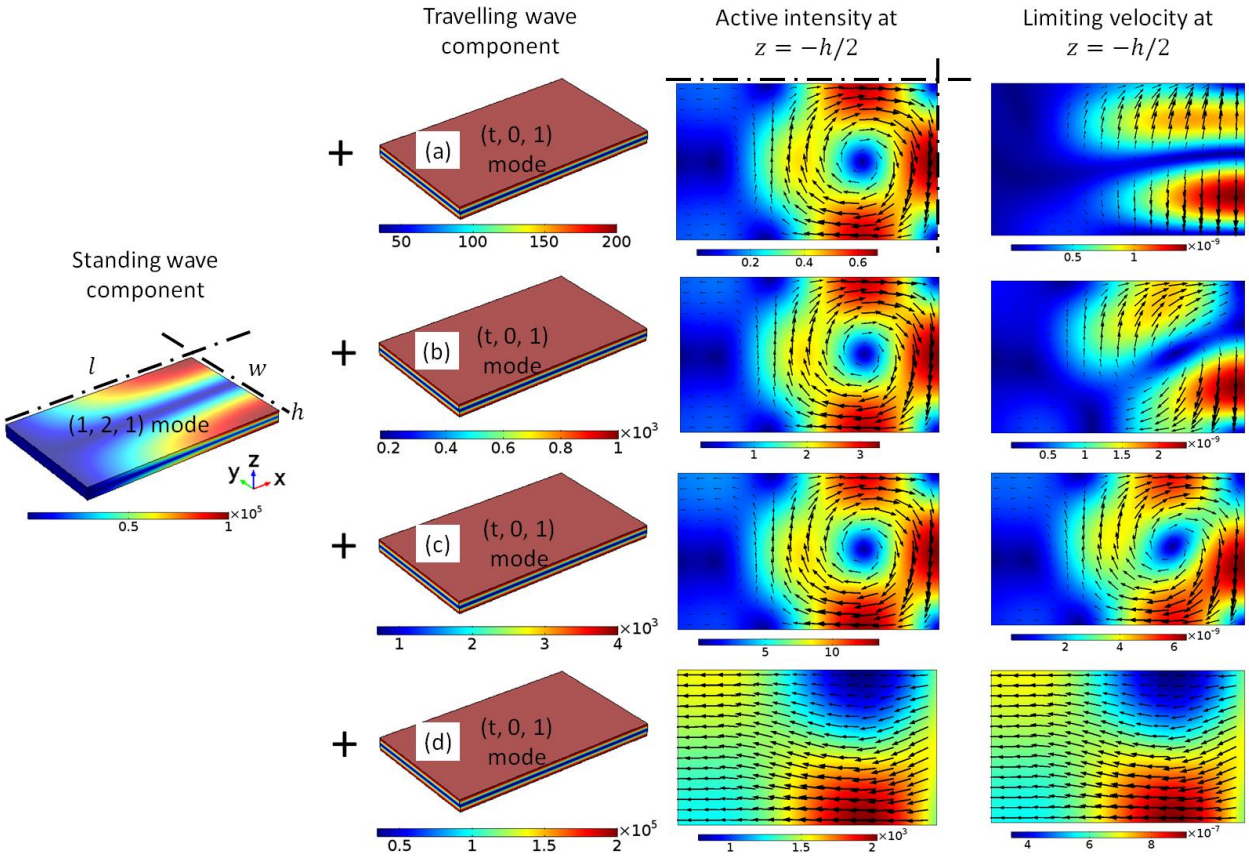

FIG. 3 The active intensity (W/m^2) and limiting velocity (m/s) fields at the driving boundaries for a number of standing and travelling wave components (Pa). The phase difference between the standing and travelling wave components, $\varphi = -\pi/2$.

excited, and it is interesting to note that the travelling wave modes (t, n, 0) do not produce transducer-plane streaming, and the higher order mode (t, 1, 1) can produce rotation in the opposite direction. Real devices will exhibit complex patterns and mode combinations that are less idealised than those presented here, but we suspect that the higher order modes are less likely to be exhibited in experimental devices.

FIG 3 shows the transitions of streaming patterns from various ratios of standing and travelling wave pressure amplitudes. For very small values of p_{0t}, modal Rayleigh-like streaming patterns [50] are seen (FIG. 3(a)). As p_{0t} increases, a gradual transition to the transducer-plane pattern is seen (FIG. 3(b-c)). Ultimately as p_{0t} approaches p_{0s}, irrotational terms become more dominant, leading to limiting velocities which follow the predominantly x-directed active intensity of the travelling wave (FIG. 3(d)), which would drive flow if the end boundaries are allowed for the passage of fluid.

For this specific mode, the limiting velocity (and hence the magnitude of the transducer-plane streaming vortices) is found to be approximately proportional (to within 5%) to that of the active intensity following (see derivation in the supplemental material [52])

$$|I|_{max} \approx \frac{k_{xt} p_{0t}^2}{2\rho_0 \omega}\left(1 + \frac{p_{0s}}{p_{0t}}\right). \qquad (5)$$

For $p_{0t} < p_{0s}$, increasing p_{0t} shifts the vortex centre outwards in the y-direction, while much larger values create a pattern resembling the uniform active intensity which follows the direction of propagation of the now dominant travelling wave component. It was also found that introducing a phase difference between the standing and travelling wave components, φ, shifts the vortex in the x-direction.

We also note that the model shows that in situations where the travelling wave component is dominant, the limiting velocity at the boundary is non-zero. This will drive a streaming pattern in addition to the (typically higher velocity) Eckart streaming which will also be present in these cases. Combinations of travelling waves in the x-direction with standing modes in z (or a pure travelling wave field) reveal that the limiting velocity can take the opposite direction to Eckart streaming in these cases, leading to streaming vortices near the boundaries (see FIG. S3 in the supplemental material [52]), as has been seen in a surface acoustic wave device where the thickness of the fluid is at or less than the viscous penetration depth [59].

In conclusion, we have demonstrated that a wider range of transducer-plane streaming patterns exist other than the four-quadrant pattern that had been observed previously, related to higher order cavity modes. As an example, a new pattern, eight-octant transducer-plane streaming, is both predicted numerically and found experimentally in a glass capillary device. We have created a simplified analytical model to provide a deeper insight into the underlying physics of transducer-plane streaming patterns in thin-layered

acoustofluidic devices. The model highlights the importance of having both standing and (typically smaller) travelling wave components present within the acoustic cavity to create rotational motion in the limiting velocity and resulting streaming fields. We show that the limiting velocity method also predicts the rotational streaming found from other acoustic vortices. The model also highlights how fields with stronger travelling wave components also exhibit boundary driven streaming creating limiting velocities at the boundaries which would not be found from pure Eckart streaming, and that interactions between boundary-driven streaming and Eckart streaming could create inner streaming vortices.

This work was supported by the EPSRC/University of Southampton Doctoral Prize Fellowship EP/N509747/1. PGJ also acknowledges support from EPSRC Fellowship EP/L025035/1. Models used to generate the simulation data, and experimental data supporting this study are openly available from the University of Southampton repository at http://doi.org/10.5258/SOTON/D0119

*andyleiapply@gmail.com
†m.hill@soton.ac.uk
‡p.glynne-jones@soton.ac.uk

[1] B. Hammarstrom, T. Laurell, and J. Nilsson, Seed particle-enabled acoustic trapping of bacteria and nanoparticles in continuous flow systems, Lab Chip **12**, 4296 (2012).
[2] B. Hammarstrom, B. Nilson, T. Laurell, J. Nilsson, and S. Ekstrom, Acoustic Trapping for Bacteria Identification in Positive Blood Cultures with MALDI-TOF MS, Analytical chemistry **86**, 10560 (2014).
[3] S. K. Chung and S. K. Cho, On-chip manipulation of objects using mobile oscillating bubbles, J Micromech Microeng **18**, 125024 (2008).
[4] B. R. Lutz, J. Chen, and D. T. Schwartz, Hydrodynamic tweezers: 1. Noncontact trapping of single cells using steady streaming microeddies, Analytical chemistry **78**, 5429 (2006).
[5] S. Yazdi and A. M. Ardekani, Bacterial aggregation and biofilm formation in a vortical flow, Biomicrofluidics **6**, 044114 (2012).
[6] M. Antfolk, P. B. Muller, P. Augustsson, H. Bruus, and T. Laurell, Focusing of sub-micrometer particles and bacteria enabled by two-dimensional acoustophoresis, Lab Chip **14**, 2791 (2014).
[7] C. Wang, S. V. Jalikop, and S. Hilgenfeldt, Size-sensitive sorting of microparticles through control of flow geometry, Appl Phys Lett **99**, 034101 (2011).
[8] C. Devendran, I. Gralinski, and A. Neild, Separation of particles using acoustic streaming and radiation forces in an open microfluidic channel, Microfluidics and Nanofluidics **17**, 879 (2014).
[9] M. Nabavi, K. Siddiqui, and J. Dargahi, Effects of transverse temperature gradient on acoustic and streaming velocity fields in a resonant cavity, Appl Phys Lett **93**, 051902 (2008).
[10] B. G. Loh, S. Hyun, P. I. Ro, and C. Kleinstreuer, Acoustic streaming induced by ultrasonic flexural vibrations and associated enhancement of convective heat transfer, J Acoust Soc Am **111**, 875 (2002).
[11] S. Hyun, D. R. Lee, and B. G. Loh, Investigation of convective heat transfer augmentation using acoustic streaming generated by ultrasonic vibrations, Int J Heat Mass Tran **48**, 703 (2005).
[12] M. K. Aktas, B. Farouk, and Y. Q. Lin, Heat transfer enhancement by acoustic streaming in an enclosure, J Heat Trans-T Asme **127**, 1313 (2005).
[13] W. Kim, T. H. Kim, J. Choi, and H. Y. Kim, Mechanism of particle removal by megasonic waves, Appl Phys Lett **94**, 081908 (2009).
[14] E. Maisonhaute, C. Prado, P. C. White, and R. G. Compton, Surface acoustic cavitation understood via nanosecond electrochemistry. Part III: shear stress in ultrasonic cleaning, Ultrason Sonochem **9**, 297 (2002).
[15] S. K. R. S. Sankaranarayanan, S. Cular, V. R. Bhethanabotla, and B. Joseph, Flow induced by acoustic streaming on surface-acoustic-wave devices and its application in biofouling removal: A computational study and comparisons to experiment, Phys Rev E **77**, 066308 (2008).
[16] A. A. Busnaina, I. I. Kashkoush, and G. W. Gale, An Experimental-Study of Megasonic Cleaning of Silicon-Wafers, J Electrochem Soc **142**, 2812 (1995).
[17] M. Keswani, S. Raghavan, P. Deymier, and S. Verhaverbeke, Megasonic cleaning of wafers in electrolyte solutions: Possible role of electro-acoustic and cavitation effects, Microelectron Eng **86**, 132 (2009).
[18] D. Ahmed, X. L. Mao, J. J. Shi, B. K. Juluri, and T. J. Huang, A millisecond micromixer via single-bubble-based acoustic streaming, Lab Chip **9**, 2738 (2009).
[19] K. Sritharan, C. J. Strobl, M. F. Schneider, A. Wixforth, and Z. Guttenberg, Acoustic mixing at low Reynold's numbers, Appl Phys Lett **88**, 054102 (2006).
[20] R. Shilton, M. K. Tan, L. Y. Yeo, and J. R. Friend, Particle concentration and mixing in microdrops driven by focused surface acoustic waves, J Appl Phys **104**, 014910 (2008).
[21] T. D. Luong, V. N. Phan, and N. T. Nguyen, High-throughput micromixers based on acoustic streaming induced by surface acoustic wave, Microfluidics and Nanofluidics **10**, 619 (2011).
[22] T. Frommelt, M. Kostur, M. Wenzel-Schafer, P. Talkner, P. Hanggi, and A. Wixforth, Microfluidic mixing via acoustically driven chaotic advection, Phys Rev Lett **100**, 034502 (2008).
[23] R. H. Liu, J. N. Yang, M. Z. Pindera, M. Athavale, and P. Grodzinski, Bubble-induced acoustic micromixing, Lab Chip **2**, 151 (2002).
[24] G. G. Yaralioglu, I. O. Wygant, T. C. Marentis, and B. T. Khuri-Yakub, Ultrasonic mixing in microfluidic channels using integrated transducers, Analytical chemistry **76**, 3694 (2004).
[25] M. K. Tan, L. Y. Yeo, and J. R. Friend, Rapid fluid flow and mixing induced in microchannels using surface acoustic waves, Epl-Europhys Lett **87**, 47003 (2009).
[26] D. Ahmed, X. L. Mao, B. K. Juluri, and T. J. Huang, A fast microfluidic mixer based on acoustically driven sidewall-trapped microbubbles, Microfluidics and Nanofluidics **7**, 727 (2009).
[27] C. Suri, K. Takenaka, Y. Kojima, and K. Koyama, Experimental study of a new liquid mixing method using acoustic streaming, J Chem Eng Jpn **35**, 497 (2002).
[28] B. Moudjed, V. Botton, D. Henry, S. Millet, J. P. Garandet, and H. Ben Hadid, Oscillating acoustic streaming jet, Appl Phys Lett **105**, 184102 (2014).
[29] R. H. Nilson and S. K. Griffiths, Enhanced transport by acoustic streaming in deep trench-like cavities, J Electrochem Soc **149**, G286 (2002).
[30] T. Maturos *et al.*, Enhancement of DNA hybridization under acoustic streaming with three-piezoelectric-transducer system, Lab Chip **12**, 133 (2012).
[31] P. H. Huang *et al.*, A reliable and programmable acoustofluidic pump powered by oscillating sharp-edge structures, Lab Chip **14**, 4319 (2014).

[32] D. Moller, T. Hilsdorf, J. T. Wang, and J. Dual, Acoustic Streaming Used to Move Particles in a Circular Flow in a Plastic Chamber, Aip Conf Proc **1433**, 775 (2012).
[33] R. M. Moroney, R. M. White, and R. T. Howe, Microtransport Induced by Ultrasonic Lamb Waves, Appl Phys Lett **59**, 774 (1991).
[34] N. Li, J. H. Hu, H. Q. Li, S. Bhuyan, and Y. J. Zhou, Mobile acoustic streaming based trapping and 3-dimensional transfer of a single nanowire, Appl Phys Lett **101**, 093113 (2012).
[35] M. Miansari and J. R. Friend, Acoustic Nanofluidics via Room-Temperature Lithium Niobate Bonding: A Platform for Actuation and Manipulation of Nanoconfined Fluids and Particles, Adv Funct Mater **26**, 7861 (2016).
[36] M. Wiklund, R. Green, and M. Ohlin, Acoustofluidics 14: Applications of acoustic streaming in microfluidic devices, Lab Chip **12**, 2438 (2012).
[37] H. Bruus, Acoustofluidics 10: Scaling laws in acoustophoresis, Lab Chip **12**, 1578 (2012).
[38] Lord Rayleigh, On the circulation of air observed in Kundt's tube, and on some allied acoustical problems., Phil. Trans. **175**, 1 (1884).
[39] H. Schlichting, Berechnung ebener periodischer Grenzschichtstromungen (Calculation of plane periodic boundary layer streaming), Physikalische Zeitschrift **33**, 327 (1932).
[40] P. J. Westervelt, The theory of steady rotational flow generated by a sound field, J. Acoust. Soc. Am. **25**, 60 (1952).
[41] W. L. Nyborg, Acoustic streaming near a boundary, J. Acoust. Soc. Am. **30**, 329 (1958).
[42] J. Lighthill, Acoustic Streaming, J Sound Vib **61**, 391 (1978).
[43] M. F. Hamilton, Y. A. Ilinskii, and E. A. Zabolotskaya, Acoustic streaming generated by standing waves in two-dimensional channels of arbitrary width, J Acoust Soc Am **113**, 153 (2003).
[44] S. S. Sadhal, Acoustofluidics 13: Analysis of acoustic streaming by perturbation methods Foreword, Lab Chip **12**, 2292 (2012).
[45] M. K. Aktas and B. Farouk, Numerical simulation of acoustic streaming generated by finite-amplitude resonant oscillations in an enclosure, J Acoust Soc Am **116**, 2822 (2004).
[46] P. B. Muller, R. Barnkob, M. J. H. Jensen, and H. Bruus, A numerical study of microparticle acoustophoresis driven by acoustic radiation forces and streaming-induced drag forces, Lab Chip **12**, 4617 (2012).
[47] P. B. Muller, M. Rossi, A. G. Marin, R. Barnkob, P. Augustsson, T. Laurell, C. J. Kahler, and H. Bruus, Ultrasound-induced acoustophoretic motion of microparticles in three dimensions, Phys Rev E **88**, 023006 (2013).
[48] J. Lei, M. Hill, and P. Glynne-Jones, Numerical simulation of 3D boundary-driven acoustic streaming in microfluidic devices, Lab Chip **14**, 532 (2014).
[49] J. Lei, P. Glynne-Jones, and M. Hill, Acoustic streaming in the transducer plane in ultrasonic particle manipulation devices, Lab Chip **13**, 2133 (2013).
[50] J. J. Lei, P. Glynne-Jones, and M. Hill, Modal Rayleigh-like streaming in layered acoustofluidic devices, Phys Fluids **28**, 012004 (2016).
[51] F.J.Fahy, *Sound intensity* (E & FN Spon, London, 1995), Second Edition edn.
[52] mpiv - MATLAB PIV Toolbox, http://www.oceanwave.jp/softwares/mpiv/.
[53] See supplemental information at [URL will be inserted by publisher] for the experimental method, numerical method, derivation of active intensities and additional streaming patterns.
[54] COMSOL Multiphysics 4.4, (COMSOL Multiphysics 4.4) http://www.comsol.com/.
[55] J. Lei, Formation of inverse Chladni patterns in liquids at microscale: roles of acoustic radiation and streaming-induced drag forces, Microfluidics and Nanofluidics **21**, 50 (2017).
[56] J. A. Mann, J. Tichy, and A. J. Romano, Instantaneous and Time-Averaged Energy-Transfer in Acoustic Fields, J Acoust Soc Am **82**, 17 (1987).
[57] R. V. Waterhouse, D. G. Crighton, and J. E. Ffowcs-Williams, A Criterion for an Energy Vortex in a Sound Field, J Acoust Soc Am **81**, 1323 (1987).
[58] Z. Y. Hong, J. Zhang, and B. W. Drinkwater, Observation of Orbital Angular Momentum Transfer from Bessel-Shaped Acoustic Vortices to Diphasic Liquid-Microparticle Mixtures, Phys Rev Lett **114**, 214301 (2015).
[59] A. R. Rezk, O. Manor, L. Y. Yeo, and J. R. Friend, Double flow reversal in thin liquid films driven by megahertz-order surface vibration, P Roy Soc a-Math Phy **470**, 20130765 (2014).